Original Article

Intracranial pressure–based validation and analysis of traumatic brain injury using a new three-dimensional finite element human head model

Tanu Khanuja[1] and Harikrishnan Narayanan Unni[2] (iD)

Abstract

Traumatic brain injuries are life-threatening injuries that can lead to long-term incapacitation and death. Over the years, numerous finite element human head models have been developed to understand the injury mechanisms of traumatic brain injuries. Many of these models are erroneous and used ellipsoidal or spherical geometries to represent brain. This work is focused on the development of high-quality, comprehensive three-dimensional finite element human head model with accurate representation of cerebral sulci and gyri structures in order to study traumatic brain injury mechanisms. Present geometry, predicated on magnetic resonance imaging data consist of three rudimentary components, that is, skull, cerebrospinal fluid with the ventricular system, and the soft tissues comprising the cerebrum, cerebellum, and brain stem. The brain is modeled as a hyperviscoelastic material. Meshed model with 10 nodes modified tetrahedral type element (C3D10M) is validated against two cadaver-based impact experiments by comparing the intracranial pressures at different locations of the head. Our results indicate a better agreement with cadaver results, specifically for the case of frontal and parietal intracranial pressure values. Existing literature focuses mostly on intracranial pressure validation, while the effects of von Mises stress on brain injury are not analyzed in detail. In this work, a detailed interpretation of neurological damage resulting from impact injury is performed by analyzing von Mises stress and intracranial pressure distribution across numerous segments of the brain. A reasonably good correlation with experimental data signifies the robustness of the model for predicting injury mechanisms based on clinical predictions of injury tolerance criteria.

Introduction

Head is a vital component of the body, impact to which may cause rigorous life-threatening injuries and can lead to long-term incapacitation and death. It is not yet completely understood how an external mechanical impact on the head leads to traumatic brain injury (TBI). In addition, it is not always possible to record the in vivo replications from a human head under the impact conditions. Over the years, numerous numerical models of the human head have been developed to understand the skull fracture and injury mechanism in the brain.[1–5] TBI affects a huge amount of the global population, ranging from mild TBI (concussion) to coma. Globally, 50 million people are injured every year with a projected death count of 1.2 million.[6] According to a study performed by the World Health Organization (WHO) in developing countries, the mortality rate due to TBI will increase by 80% by 2020.[7] Recent advancements in the field of biomechanics of TBI suggest finite element analysis (FEA) as an effective tool to understand the brain injury mechanism. FEA emphasizes the impact of replication and injury

[1]Department of Biomedical Engineering, Indian Institute of Technology Hyderabad, Hyderabad, India
[2]Biomicrofluidics and Biomechanics Lab, Department of Biomedical Engineering, Indian Institute of Technology Hyderabad, Hyderabad, India

Corresponding author:
Harikrishnan Narayanan Unni, Biomicrofluidics and Biomechanics Lab, Department of Biomedical Engineering, Indian Institute of Technology Hyderabad, Kandi, Sangareddy District, Hyderabad 502285, Telangana, India.
Email: harikrishnan@iith.ac.in

threshold criteria in the intricate head structure.[8,9] In recent years, researchers have generated a number of head models to study TBI mechanism. However, many of these models are erroneous and used ellipsoidal and spherical geometries to represent brain. The shape of the cerebrum is approximated to a sphere, without clear representation of gyri and sulci structures on the brain surface.[1,3,5,10–14] One of the earliest models[15] used a spherical liquid mass model to represent head where simple boundary conditions with homogeneous material properties were assumed, and coup and contre-coup pressures were observed. Subsequently, a number of intricate three-dimensional (3D) models were reported, resulting in an improved understanding of TBI mechanics.[16–25] Some of the complex models representing the gyri and sulci structures in the brain are developed recently.[26,27] Majority of the models reported in the literature[10,11,27] are validated only against the experimental data presented by Nahum et al.[28] Therefore, there still exist a need for the generation of high bio-fidelity human head models and validation against multiple cadaver-based experimental data, in order to understand injury mechanisms comprehensively. The human head primarily consists of the skull, cerebrospinal fluid (CSF), cerebrum, cerebellum, brain stem, and meningeal layers. The skull bone is a three-layered sandwich structure with a spongy bone sandwiched between the inner and outer layers of compact bone. The thickness of the human skull varies from 3 to 10 mm with a mean ranging between 5 and 7 mm. In addition, skull thickness depends on the gender and age of the subject as well.[29] The occipital bone of the skull has a considerably voluminous oval opening in the base, called foramen magnum which connects brain stem to the spinal cord. The brain tissue can be compared to a soft gel because of the high water content (about 80%). CSF of average thickness ranging from 0.25 to 5 mm circumvents these tissues.[30,31] Blow to the head instigates damage to the brain, which results in minor to major TBI. Clinically, TBI is classified into two broad categories, that is, focal injury and diffuse injury. Focal injury results from direct impact, typically when an object perforates the skull as a result of accidents. Diffuse injury is the result of traumatic shearing forces that arise when the head is rapidly accelerated or decelerated. Contusion and concussion are the most commonly diagnosed TBI, where immediate loss of consciousness is reported.[32] These phenomena contribute to bruises and blood clotting on the outer surface and inner volume of the brain. The gyri and sulci folds present on the surface of cerebral hemispheres increase the surface area of the brain. These folds limit the extent of brain damage resulting from blunt impacts. Therefore, it is important that surface of brain soft tissue is accurately represented, in order to study and understand the injury mechanisms. There are only a few cadaver-based experiments reported in the literature[4,28,33–36] that can be used to validate the finite element (FE) human head models. A thoroughly validated model can be used for prediction of injuries resulting from different types of impact, and this will be helpful in designing suitable head-protective gears. It has been an immense challenge for the researchers to define a perfect material model for biological tissues. A majority of researchers have used viscoelastic and hyperviscoelastic material properties for the brain from restricted experimental data reported in the literature.[30,37–40]

In this article, we discuss an FE human head model where cerebral surfaces are accurately represented. The model consists of skull with foramen magnum, CSF with ventricular system, and soft tissues comprising cerebrum, cerebellum, and brain stem. The developed model is validated against two cadaver-based experiments.[28,33] Maximum intracranial pressure (ICP) and von Mises stress across different segments of the brain are studied in detail, and possible neurological implications are elaborated. According to Suwatcharangkoon et al.,[41] increase in ICP causes transient interruption of blood flow in cerebral tissue, and this leads to a sudden loss of consciousness. Therefore, the probability of loss of consciousness is identified using ICP as an indicator. Existing literature is focused primarily on ICP validation and calculation of relative displacements between intracranial organs, while lesser emphasis has been placed on determining the effect of von Mises stress and corresponding neurological damage in the interior of the brain. The von Mises stress correlates better with the probability of neurological lesion formations.[42] In this study, von Mises stress distribution across brain slices is calculated, and the probability of cerebral damage is discussed in detail.

Method

Head model generation

Computed tomography (CT) and magnetic resonance imaging (MRI) represents the finest imaging modalities that are used to diagnose TBI. Multi-planar imaging capability, sensitivity, and precision in diagnosing cerebral pathology make MRI superior to CT.[43] The T1-weighted cross-sectional MRI obtained from IMAIOS[44] is used to generate 3D FE human head model. Individual images consist of pixel details of 320/320 matrix which are obtained using a 1.3-Tesla MRI machine. The model is reconstructed in image predicated meshing commercial software AMIRA 5.6. Model segmentation is performed by identifying and labeling the regions of interest (ROIs) within the grey-scale data. The segmented images consist of three label fields, namely, brain (including the cerebrum, cerebellum, and brain stem), CSF (including ventricles), and skull with foramen magnum. CSF layer is labeled in the accumulation with the meningeal layers. For labeling the ROI during segmentation, we have used manual and semi-automated implements such as manual brush (painting), lasso (contouring), magic wand (region-
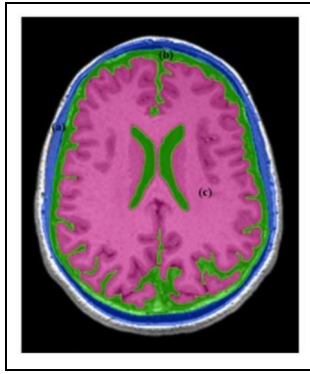
Figure 1. Illustration of segmented labels in a transaxial slice: (a) skull, (b) CSF, and (c) cerebrum.

growing), thresholding, intelligent scissors, contour-fitting (snakes), contour interpolation and extrapolation, wrapping, smoothing, and de-noising filters. Manual interaction is avoided using threshold segmentation.

Image filters such as "smooth labels" and "remove islands" are employed for smoothening the surface within the masks and filling the cavities. Figure 1 illustrates the segmented labels ((a) skull, (b) CSF, and (c) brain) in a transaxial slice of MRI. Figure 2 illustrates the segmented volumes of the complete model. The sulci and gyri structures are accurately maintained during model reconstruction. All cerebral lobes are clearly

visible in the segmented structure of the brain (Figure 2(d)–(f)). The width of the brain from the frontal lobe to occipital lobe is measured as 16.2 cm, length from top of the parietal lobe to the bottom of the occipital lobe is 10.5 cm, and the distance from left to right temporal lobe is 13.09 cm. The brain comprises a volume of 1421 cm³, lying in the range reported by Allen et al.[45] CSF and dura mater are modeled as a single layer. Skull thickness varies between 3 and 10 mm which satisfies the thickness reported by Ruan and Prasad.[29]

Mesh generation

It has been a challenge in FEA to generate the volume mesh from a complex three-dimensional model which is developed using CAD software. The majority of the models developed in the past have avoided the complexity of the brain due to the inability of FE solvers to convert the CAD files into compatible formats. In addition, a high amount of manual editing of the geometry eventually results in losing the geometrical complexity of cerebral structures. In order to maintain the accuracy of the model, semi-automatic meshing is performed with the marching cube algorithm in AMIRA 5.6. The surfaces of different label fields are reduced to the STL format comprising 0.1 million triangular faces. Mesh quality is maintained by adjusting parameters such as triangle aspect ratio, dihedral angle, and orientation by manually editing the edges and faces of the
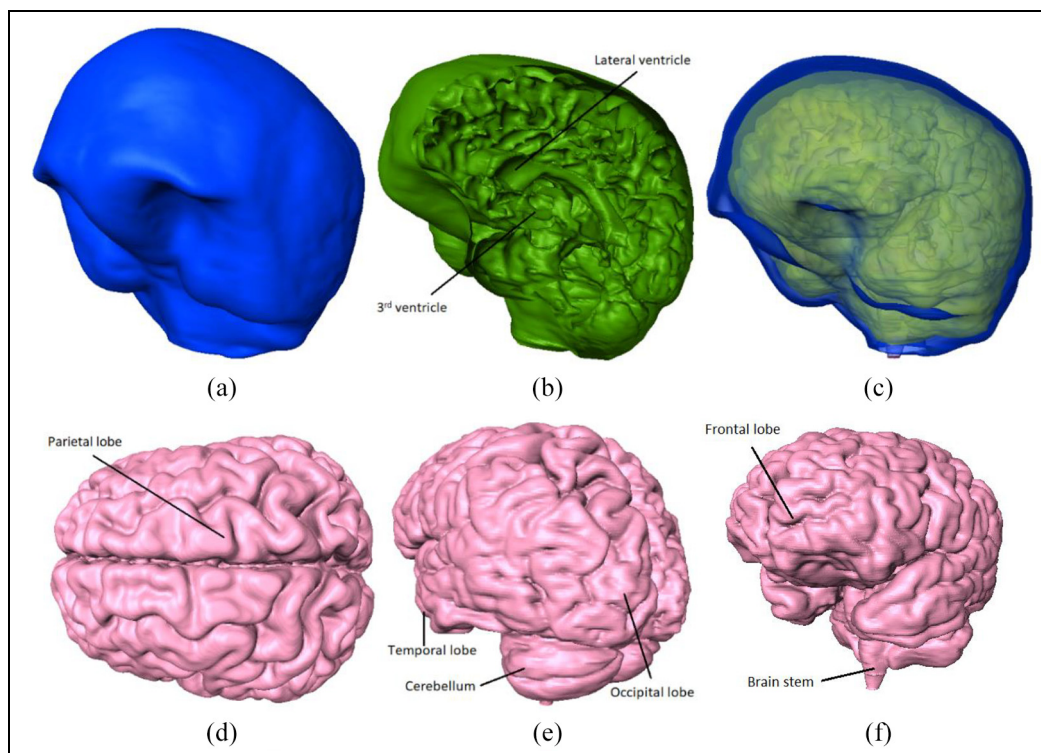

Figure 2. Illustration of segmented parts in head model representing: (a) skull; (b) CSF circulating around brain and inside ventricles; (c) full head transparent model; (d) top view of cerebrum with representation of gyri and sulci; (e) posterior view of cerebrum with representation of cerebellum, occipital lobe, and temporal lobe; and (f) front view of cerebrum with representation of brain stem and frontal lobe.
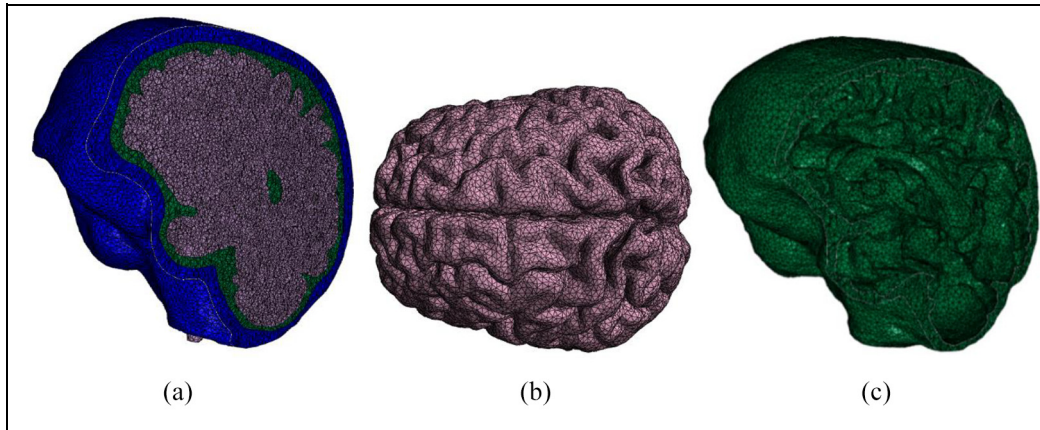
Figure 3. Illustration of meshed parts of the model: (a) cross-sectional view of full meshed head model with 1.08 million C3D10M elements, (b) brain meshed with 662,113 C3D10M elements, and (c) CSF meshed with 176,351 C3D10M elements.

triangles. According to Baumgartner and Willinger,[42] the calculated values of ICP depend on the type of skull–brain interface, and the tied interface provides the best result. Therefore, meshing is performed with shared (tied) nodes between individual segments in AMIRA 5.6. Bad tetrahedral elements are repaired by smoothening tools such as Laplace, optimization, and combined smoothening. The meshed model is imported to Abaqus 6.9/Explicit FE solver without compromising the model complexity. It is observed that four nodes tetrahedral (C3D4) elements result in hourglassing during simulations (this means some individual elements get severely deformed while surrounding elements remains undeformed). This is caused by the presence of zero-energy degrees of freedom in the model which produces false deformation mode of FE mesh. Therefore, the linear four-node tetrahedral element formulation (C3D4) is modified to nonlinear 10-node tetrahedral element formulation (C3D10M) in Abaqus 6.9/Explicit. The mesh density is optimized by performing the simulation using different mesh density models (0.534 million, 0.747 million, and 1.008 million mesh elements). This step is performed to confirm that the numerical results are independent of the choice of mesh density. A minimal difference in ICP values (1.28%) is observed between 0.747 million and 1.008 million element models. The optimized model includes a total of 1.008 million C3D10M elements. All segments of the meshed model are illustrated in Figure 3. Figure 3(a)–(c) illustrates the following: the complete meshed model, top view of the meshed cerebrum, and cross-sectional view of meshed CSF, respectively. The cerebral ventricles are clearly visible in Figure 3(c).

Material modeling

Most of the biological tissues are anisotropic, and soft tissues exhibit nonlinear elastic behavior. Ideally, CSF should be considered as a Newtonian biological fluid with homogeneous consistency similar to water (as

Table 1. Constitutive material properties used to model CSF.

Density (kg/m^3)	C_{10} (MPa)	C_{01} (MPa)	D_1 (MPa^{-1})
1000	0.9	1	0.9

99% of CSF is water).[46] However, this would necessitate the consideration of CSF dynamics, adding further complexity to the simulations. Consequently, CSF is modeled as a solid hyperelastic material as presented in Table 1.[27] CSF is represented using Mooney–Rivlin model which is a special case of the polynomial hyperelastic model. The model is mathematically expressed as follows[47]

$$W = \sum_{p,q=0}^{N} C_{pq}(\bar{I}_1 - 3)^p(\bar{I}_2 - 3)^q + \sum_{m=1}^{M} \frac{1}{D_m}(J-1)^{2m} \quad (1)$$

where W is the strain energy density function, C_{pq} is the material constant, $\bar{I}_1$ and $\bar{I}_2$ are the first and second invariants of deviatoric right Cauchy deformation tensor, and J is the total volumetric ratio.

The deviatoric invariants of right Cauchy deformation tensor are derived from deviatoric principle stretches $\bar{\lambda}_i$, given by equations (2) and (3) as

$$\bar{I}_1 = J^{-2/3}I_1 = tr(\bar{C}) = \bar{\lambda}_1^2 + \bar{\lambda}_2^2 + \bar{\lambda}_3^2 \quad (2)$$

$$\bar{I}_2 = J^{-4/3}I_2 = \left((tr(\bar{C}))^2 - tr(\bar{C}^2)\right)$$
$$= \bar{\lambda}_1^2\bar{\lambda}_2^2 + \bar{\lambda}_2^2\bar{\lambda}_3^2 + \bar{\lambda}_3^2\bar{\lambda}_1^2 \quad (3)$$

where I_i is invariant of right green Cauchy deformation tensor C, related to principle stretch λ_i by equations (4) and (5)

$$I_1 = tr(C) = \lambda_1^2 + \lambda_2^2 + \lambda_3^2 \quad (4)$$

$$I_2 = \left((tr(C))^2 - tr(C^2)\right) = \lambda_1^2\lambda_2^2 + \lambda_2^2\lambda_3^2 + \lambda_3^2\lambda_1^2 \quad (5)$$

where $C = F^T F$ and F is the deformation gradient.

Table 2. Constitutive material properties used to model skull.

Density (kg/m³)	Young's modulus (E) (MPa)	Poisson's ratio (ν)
3500	6000	0.21

Table 3. Constitutive material properties used to model brain.

Density (kg/m³)	1040	
Hyperelastic coefficients	μ_1 (Pa)	12,000
	α_1	5.0507
	D_1 (Pa^{-1})	4E−008
Viscoelastic coefficients (Prony series)	g_1	0.5837
	τ_1	0.02571
	g_2	0.2387
	τ_2	0.02570

For $N = 1$, $m = 1$, and $C_{11} = 0$, the Mooney–Rivlin strain energy density function is defined as

$$W = C_{10}(\bar{I}_1 - 3) + C_{01}(\bar{I}_2 - 3) + \frac{1}{D_1}(J - 1)^2 \qquad (6)$$

where C_{10}, C_{01}, and D_1 are material parameters.

The relation between Cauchy stress σ_{ij} in the material and strain energy density function W is given by equation (7), where F_{ij} is the deformation gradient tensor

$$\sigma_{ij} = \frac{2}{J} F_{ik} \frac{\partial W}{\partial C_{kl}} F_{lj}; \quad i,j = 1, 2, 3 \qquad (7)$$

For ideally incompressible material, the volume-dependent parameter D_1 becomes zero. A small value (0.9×10^{-6}) of D_1 is chosen,[27] so that the CSF is modeled as nearly incompressible solid material.

Skull is modeled as a homogeneous linear elastic material and the properties are presented in Table 2.[48] Anisotropic material properties for the entire skull are unavailable; hence, skull is considered to be homogeneous. A single layer of skull is considered in the present model. The brain is modeled as a hyperviscoelastic material, where the soft biological tissue is considered as nearly incompressible. The hyperelastic and viscoelastic components of the brain are represented by one-term Ogden model and Prony series coefficients, respectively, as presented in Table 3.[27,30]

The Ogden strain energy density function is defined as[49]

$$W = \sum_{i=1}^{N} \frac{2\mu_i}{\alpha_i} \left(\bar{\lambda}_1^{\alpha_i} + \bar{\lambda}_2^{\alpha_i} + \bar{\lambda}_3^{\alpha_i} - 3 \right) + \sum_{i=1}^{N} \frac{1}{D_i}(J - 1)^{2i} \qquad (8)$$

where μ_i, α_i, and D_i are material constants, $\bar{\lambda}_i$ is deviatoric principle stretch, and J is total volumetric ratio.

For one-term Ogden model ($i = 1$), the strain energy density function is given by equation (9)

$$W = \frac{2\mu_1}{\alpha_1} \left(\bar{\lambda}_1^{\alpha_1} + \bar{\lambda}_2^{\alpha_1} + \bar{\lambda}_3^{\alpha_1} - 3 \right) + \frac{1}{D_1}(J - 1)^2 \qquad (9)$$

where μ_1 is given by Prony series as

$$\mu_1(t) = \mu_0 \left[1 - \sum_{k=1}^{n} g_k \left(1 - e^{-\frac{t}{\tau_k}} \right) \right] \qquad (10)$$

where g_k and τ_k are relaxation coefficient and relaxation time, respectively, and μ_0 is the short-term shear modulus.

Boundary condition

The boundary condition at the head–neck junction depends on the impact intensity. However, during a sudden impact to the head, the incognizance of the person leads to the consideration of free kineticism of the head–neck junction. Pressure releasing hole, the foramen magnum is modeled to produce more realistic numerical solutions.[50] Figure 4(a) and (b) illustrates the location of the foramen magnum, the freely moving head–neck junction, and the impact location. Model validation is performed against the two experimental data available in the literature.[28,33] Case 1 represents the validation of the model by comparing ICP values computed by our model against experimental ICP values reported by Nahum (experiment no. 37).[28] We have also compared our validation results against a recently developed FE human head model (yet another head model (YEAHM)), produced by Fernandes et al.[27] In Case 2, the ICP values computed by our model at different locations on the head are compared against the experimental ICP values measured by Trosseille in his experiment no. 428-2.[33] The result of our model is also compared with the validation result of Zhao et al.'s[1] FE human head model.

Results and discussion

Case 1: validation with Nahum's experiment no. 37

An impact force derived from Nahum et al.'s[28] experiment no. 37 is applied on the forehead to validate our model with impact boundary conditions as illustrated in Figure 4. The results are later compared with a recent "YEAHM" presented by Fernandes et al.[27] Figure 5 depicts the impact force used by our model (identical to the impact force used by Nahum for experiment no. 37) and YEAHM. As illustrated in Figure 6, location of the major components of the brain is represented in terms of slice ranges along the three cross-sectional planes. Slice ranges with corresponding brain components are collated in Table 4. The simulation is performed with an automatic time increment of 45.55 ns in Abaqus 6.9/Explicit (where minimum time increment/stability limit is the ratio of the minimum distance between element nodes of the smallest element and dilatational wave speed in the material).
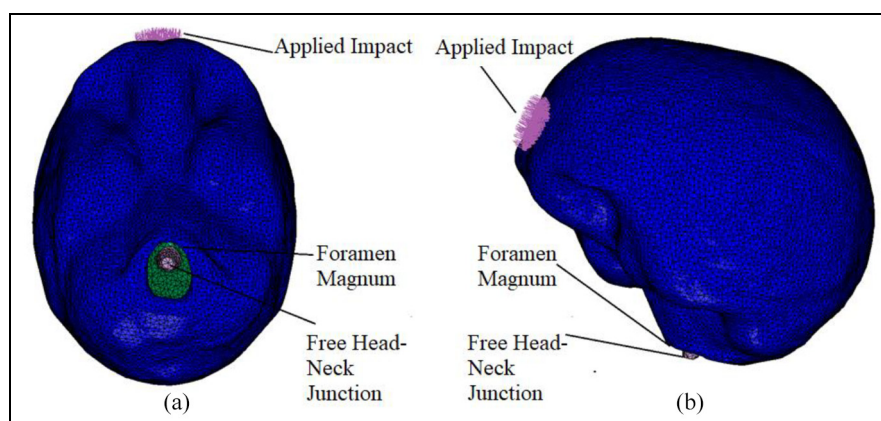
Figure 4. Illustration of impact boundary conditions used for model validation simulations: (a) foramen magnum and free head–neck junction and (b) impact location for the model validation simulations for Case 1 and Case 2.

Table 4. Slice range corresponding to major brain segments.

Brain segment (distance between adjacent slices)	Coronal slices (8.1 mm)	Sagittal slices (7.65 mm)	Transaxial slices (6.5 mm)
Frontal lobe	1–7	5–16	2–11
Parietal lobe	8–15	2–19	1–8
Occipital lobe	16–20	3–18	6–15
Cerebellum	14–19	4–17	15–19
Brain stem	10–13	8–12	15–20
Lateral ventricle	6–15	6–14	7–11
Third ventricle	14–17	9–11	9–13
Temporal lobe	5–11	1–8 and 14–20	8–12
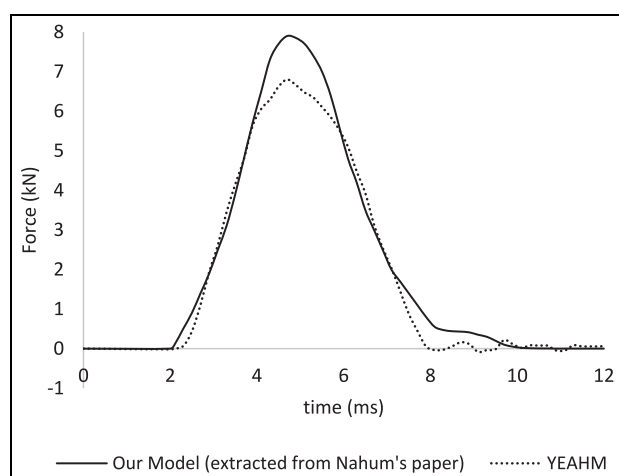
Figure 5. Illustration of the input force in model validation simulations for Case 1.

Figure 6. Illustration of cross-sectional planes.

We have compared the ICP distribution with respect to time at frontal (Figure 7(a)), parietal (Figure 7(b)), occipital (Figure 7(c)), and posterior fossa (Figure 7(d)) region with Nahum's experimental results. The results indicate a good correlation between model and experiment, specifically for the frontal and parietal regions.

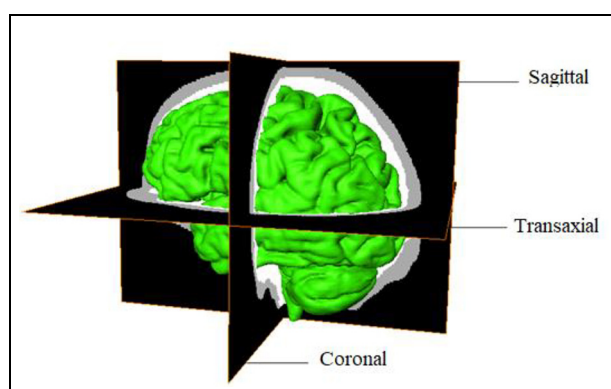Nahum evaluated the two different occipital ICPs at left and right poles of the occipital lobe. Hence, we have extracted ICP at both the poles of the occipital lobe. We observed that the ICP distribution at both the poles of the occipital lobe is same, unlike the different ICP observed by Nahum at left and right poles of the occipital lobe, as illustrated in Figure 7(c). On the contrary, the ICP distribution in our model is observed to be an approximate average of the occipital ICP measured by Nahum at two poles.

The reason behind this dissimilarity can be attributed to the variations in the head dimensions of the different human subjects and experimental conditions (i.e. conditioned or unconditioned tissue types) used in
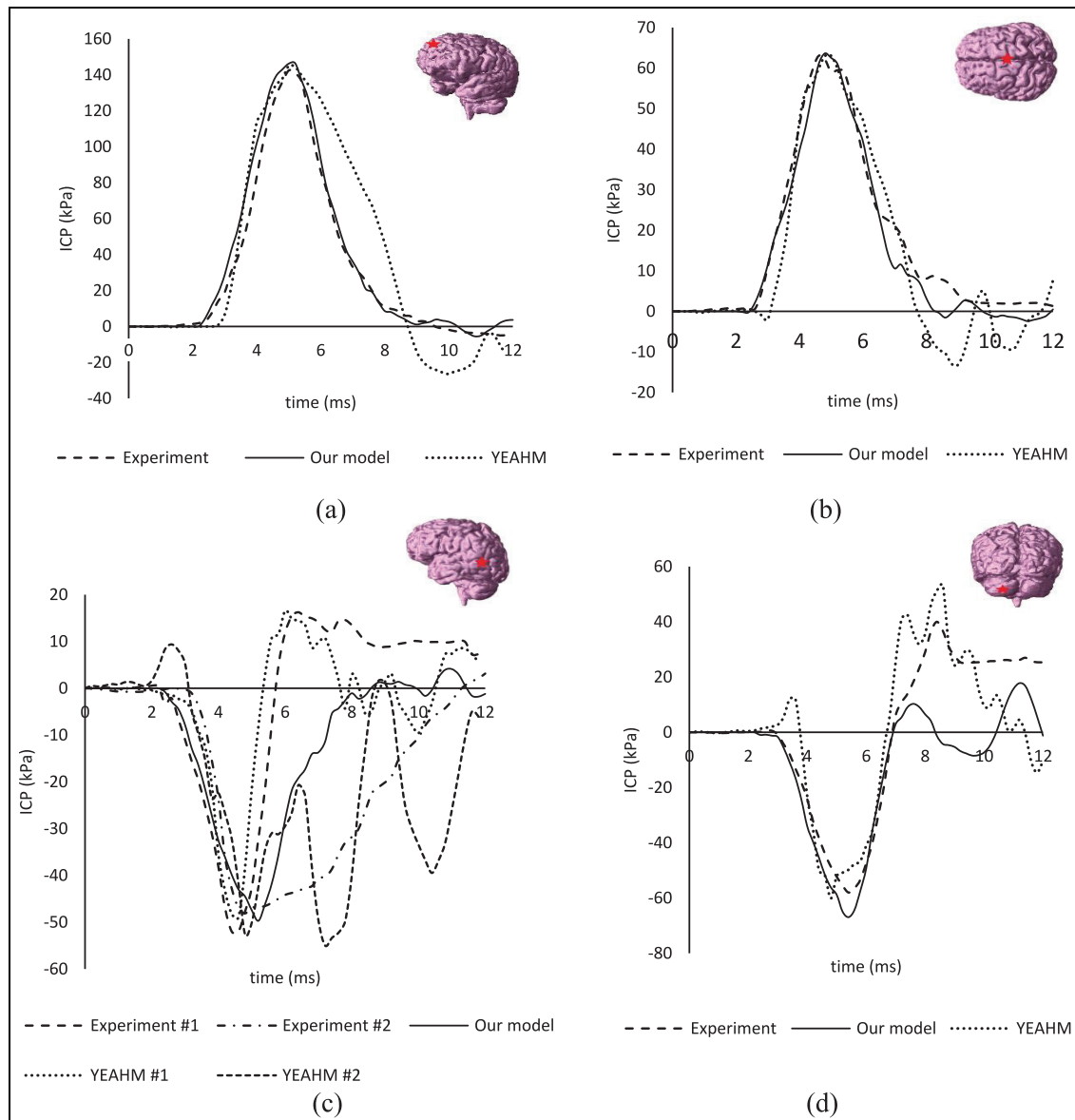
Figure 7. Illustration of comparison of ICP response from Nahum's experiment, present FE model, and YEAHM with brain legends depicting the location of ICP measured:[27] (a) frontal ICP, (b) parietal ICP, (c) occipital ICP, and (d) posterior fossa ICP.

cadaver-based experiments to calculate material properties of brain tissues. Figure 8(a) and (b) illustrates the ICP distribution across the brain where a maximum positive pressure of 146.4 kPa is observed in the frontal lobe, while a maximum negative pressure of −120 kPa is observed at the posterior center of the occipital lobe. As mentioned earlier, the occipital ICP measured by Nahum is not at the posterior center; instead, the measurements are made on two sides of the occipital lobe. Based on the peak value of Nahum's occipital ICP (i.e. −49.7 kPa at around 6 ms), the contre-coup pressure lies near the safe range of the non-injury case (i.e. −59 to −23 kPa).[51] However, based on our simulation results, the peak value of contre-coup pressure at 6 ms is −120 kPa which exceeds the range of TBI threshold (i.e. −101 to −51 kPa)[51] with a high margin of −19 kPa. This interpretation signifies the advantage of

FE simulation of TBI to precisely understand the injury severity. Furthermore, the maximum coup pressure (i.e. 146.4 kPa) as well exceeds the tolerance limit (i.e. 66 to 114 kPa)[51] to cause any type of TBI.

Our FE model simulation is in better correlation with Nahum's experimental results as compared to the recently developed FE model (YEAHM) presented by Fernandes et al.[27] The ICP values compared in Figure 7 indicates that the peak pressure values are in reasonable agreement with experimental results. In addition, our results are less oscillatory in nature as compared to the pressure slope observed in YEAHM. It should be noted that the material properties used by our model are identical to YEAHM. Furthermore, the impact force utilized by YEAHM has peak impact force less than the experimental force mentioned by Nahum in experiment no. 37.[28]
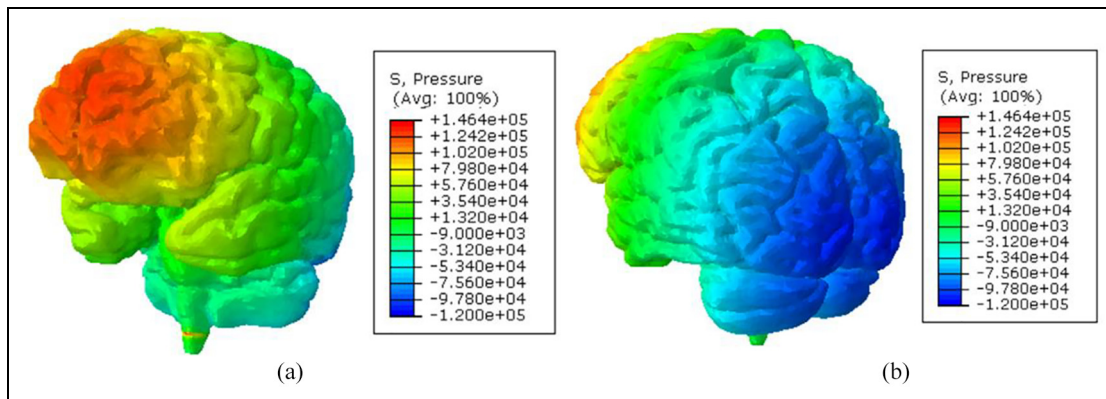
Figure 8. ICP distribution during simulation of Nahum's experiment no. 37 (Case 1): (a) anterior view and (b) posterior view.
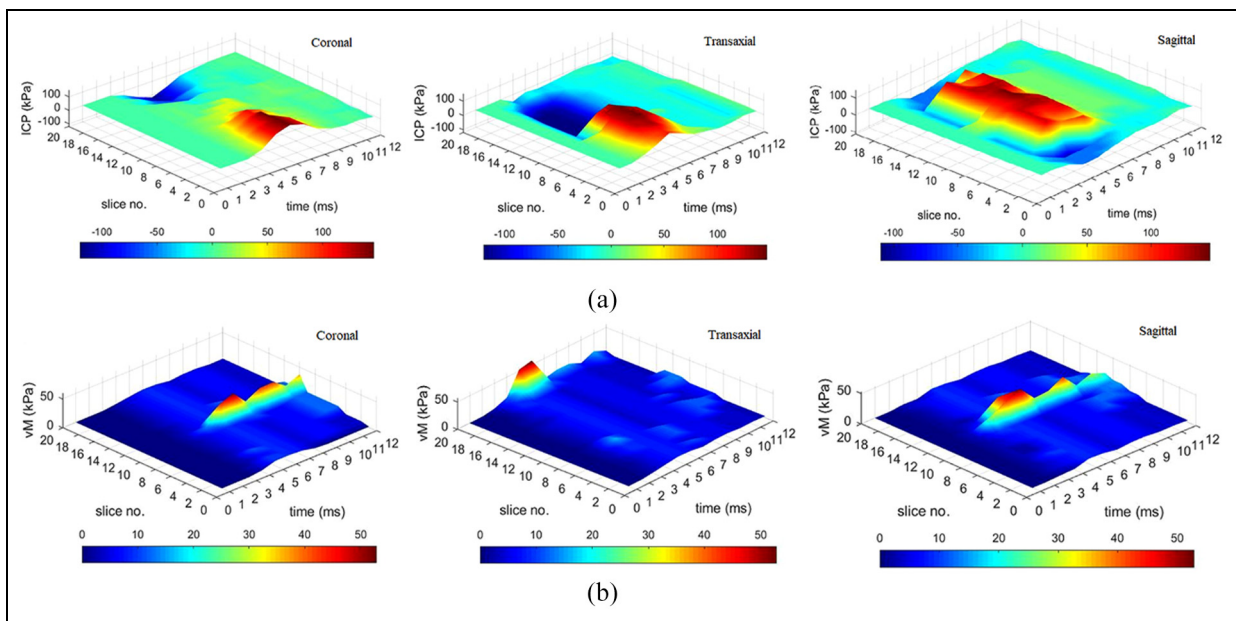

Figure 9. Illustration of the time evolution of (a) maximum ICP and (b) vM distribution with the position of brain cross-sectional slices for Case 1.

In order to understand the brain injury mechanism and corresponding neurological implications in detail, ICP and von Mises stress on different subparts of the brain should be studied. Maximum ICP and von Mises stress values are calculated at 20 cross-sectional slices in three cross-sectional planes, namely, coronal (front to the back of the brain), sagittal (left to right of the brain), and transaxial (top to bottom of the brain) plane as depicted in Figure 6. Time evolution of ICP and von Mises stress across 20 brain cross-sectional slices, each along three cross-sectional planes are presented in Figure 9(a) and (b), respectively. As depicted in Figure 9(a), ICP greater than $+100$ kPa lies in the slice range of 1–5 (coronal), 3–10 (transaxial), and 6–14 (sagittal). Furthermore, based on Table 4, the frontal lobe lies in the range common to the mentioned cross-sectional slices in the three planes. This observation indicates that the frontal lobe experiences the highest ICP across the brain. On the other hand, the highest

value of negative ICP (-120 kPa observed at the posterior center of occipital lobe) can be observed from coronal cross-sectional slices in the range of 16–20. The transaxial plot also indicates that the occipital lobe experiences the highest value of negative ICP. The coronal and transaxial ICP surface plots depict the tension (positive ICP) at the anterior side, compression (negative ICP) at the posterior side, and neutral ICP in the middle of the brain. This eventually demonstrates the occurrence of the coup, contre-coup phenomena in the brain and pressure wave propagation across the brain due to frontal impact. The sagittal surface plot indicates that maximum positive pressure is obtained near the anterior center of the frontal lobe. It also indicates approximate symmetry of pressure distribution across the sagittal cross section of the brain. The von Mises stress distribution across different brain cross sections is illustrated in Figure 9(b). The peak value of stress is observed at around 5 ms within the slice range 10–12
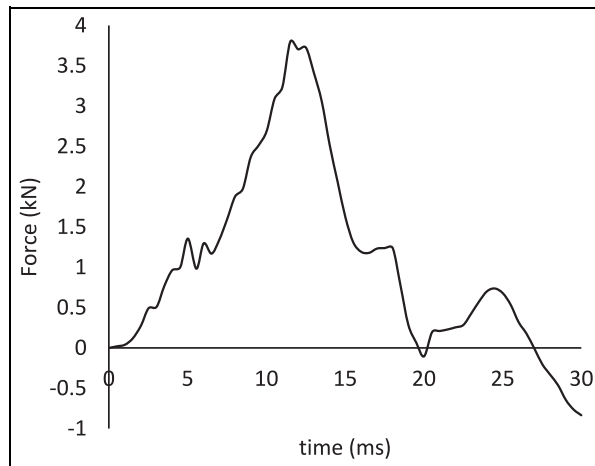
Figure 10. Illustration of the impact force used by our model for validation in Case 2.

(coronal), 10–12 (sagittal), and 18–20 (transaxial). This consists of the dorsal part of the brain stem region near foramen magnum.

According to Willinger and Baumgartner,[52] the von Mises stress surpassing 39 kPa engenders 50% probability of astringent neurological damage. In the present case, the maximum value of von Mises stress is observed to be 65.7 kPa in the brain stem. This exceeds the neuronal threshold stress, indicating a high probability of damage to brain stem tissue.

Case 2: validation with Trosseille's experiment no. 428-2

Following the validation of the model against Nahum's experiment, our FE model is validated against the Trosseille et al.'s[33] experiment no. 428-2. The impact force derived from the acceleration data given by Trosseille, as presented in Figure 10, is applied on the skull forehead where free head–neck boundary conditions are assumed.

The simulation is performed in Abaqus 6.9/Explicit with automatic time increment of 45.58 ns. The pressure response calculated is plotted at four locations on the brain, namely, frontal lobe, lateral ventricle, third

ventricle, and occipital lobe. Figure 11 illustrates the ICP distribution across the brain where Figure 11(a) and (b) depicts the positive ICP at the frontal lobe and negative ICP at the occipital lobe. The ICP distribution across third ventricle and lateral ventricle can be observed in Figure 11(c).

The validation graphs are depicted in Figure 12. As illustrated in Figure 12(a) and (d), the frontal and lateral ventricle ICP response is in reasonable agreement with experimental results till near 20 ms. In comparison with the model validation performed by Zhao et al.[1] against Trosseille's experiment no. 428-2, the peak value of the frontal ICP in our model is in better correlation with the experimental results. The variation of ICP in the third ventricle and lateral ventricle is nearly the same when comparing our results with Zhao et al.[1] As indicated in Figure 12(a), the maximum pressure in the frontal lobe is 77.1 kPa which is approximately 12% less than the experimental peak ICP. Figure 12(b) and (c) depicts the pressure distribution in the occipital lobe and third ventricle where the peak ICP values are 46.79 and 19.5 kPa, respectively. Figure 12(d) depicts the pressure distribution in lateral ventricles with a peak value of 35.7 kPa which is approximately 4.7% higher than the experimental peak ICP. The maximum negative pressure in the occipital region and the maximum positive pressure in the third ventricle is 76% higher and 44.2% lower than the corresponding experimental pressure peaks, respectively. The validation performed by most of the computational models found a high value of occipital peak pressure as compared to the experimental results. The reasons for the inconsistent result during the occipital impact can be explained by many factors like absence of meningeal layers and modeling CSF as a solid layer. The type of tissues used (i.e. unconditioned or conditioned brain tissue) during the experimental testing may also influence the results. The presence of CSF (whether present or drained out while placing sensors) in cadaver subject is not mentioned clearly in the experimental papers. As the impact is applied to the frontal region of the head, the presence of CSF between frontal and occipital lobes would result in higher peak ICP in the occipital lobe. This could be a possible reason for the higher peak value of occipital
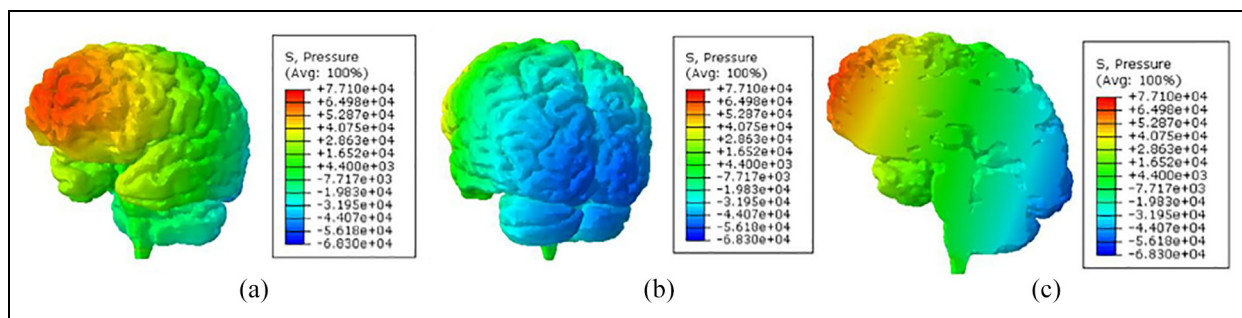

Figure 11. Peak ICP distribution during simulation of Trosseille's experiment no. 428-2 (Case 2): (a) frontal ICP, (b) occipital ICP, and (c) third ventricle and lateral ventricle ICP.
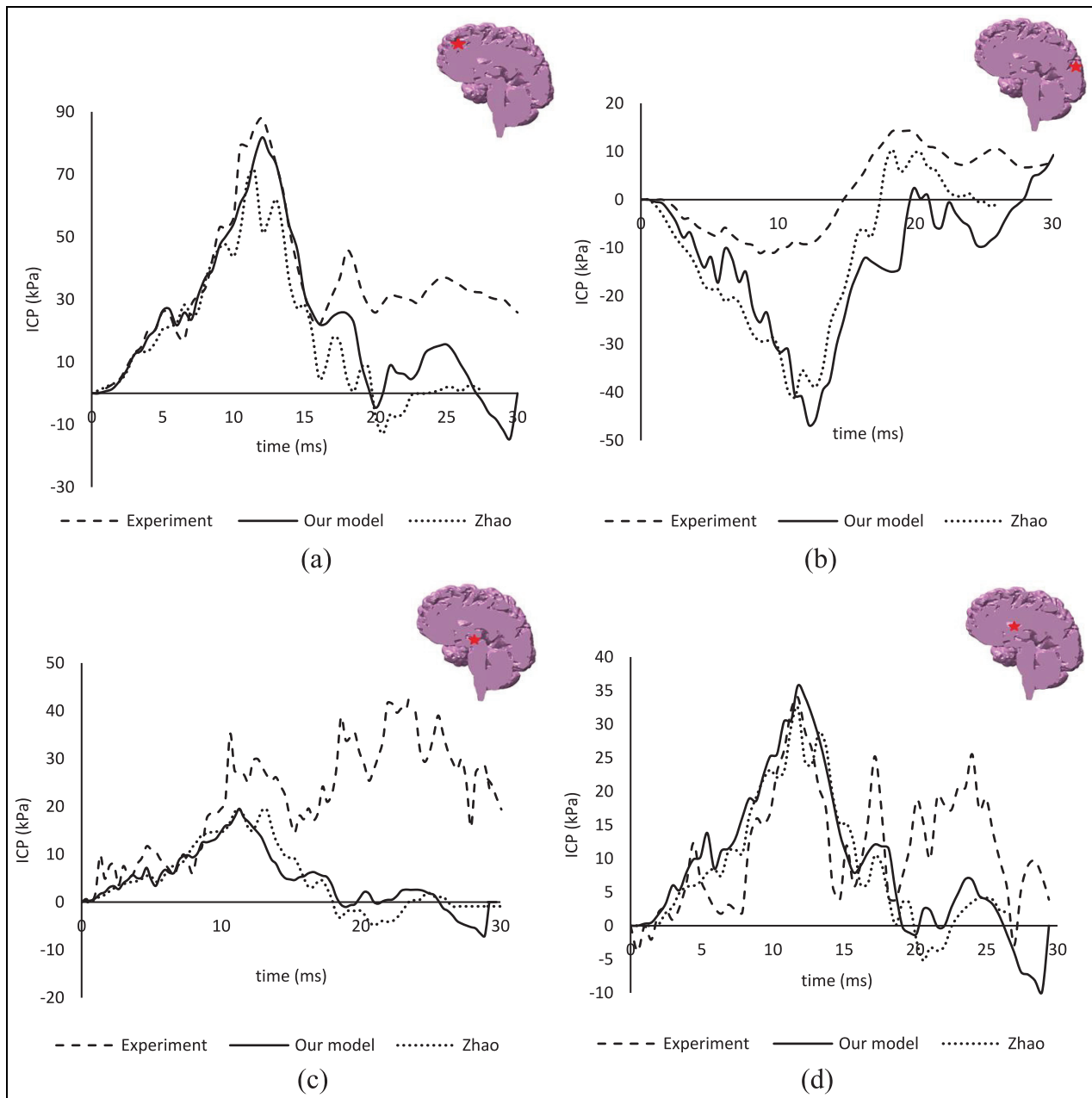
Figure 12. Illustration of comparison of ICP response from Trosseille's experiment, present FE model, and Zhao et al.'s[1] model with brain legends depicting the location of pressure measured (a) frontal ICP, (b) occipital ICP, (c) third ventricle ICP, and (d) lateral ventricle ICP.

ICP in simulation, while the difference in peak ICP (simulation versus experiment) is less pronounced in non-occipital cases. Other reasons for the mismatch between theory and experiment may include the non-consideration of the effect of anisotropy of brain tissue in the present material model. Some experiments report that the brain tissue clearly behaves anisotropically under impacts.[53–55] The effect of stress softening in brain tissues is not incorporated in the present model (corresponding to zero loads).

Similar to Case 1, the time evolution of ICP and von Mises stress across 20 brain cross-sectional slices is

depicted in Figure 13(a) and (b), respectively. The distribution pattern obtained in Case 2 is analogous to Case 1, with the exception of the values of maximum ICP and von Mises stress. The ICP distribution illustrated in Figure 13(a) shows coup and contre-coup phenomena as in Case 1. The maximum value of coup pressure lies near lower tolerance range of 66–114 kPa for mild TBI as per reported literature,[51] which predicts less probability of TBI in this case. The maximum value of von Mises stress is obtained as 52.3 kPa near the brain stem region, which represents the 50% probability of astringent neurological damage as per
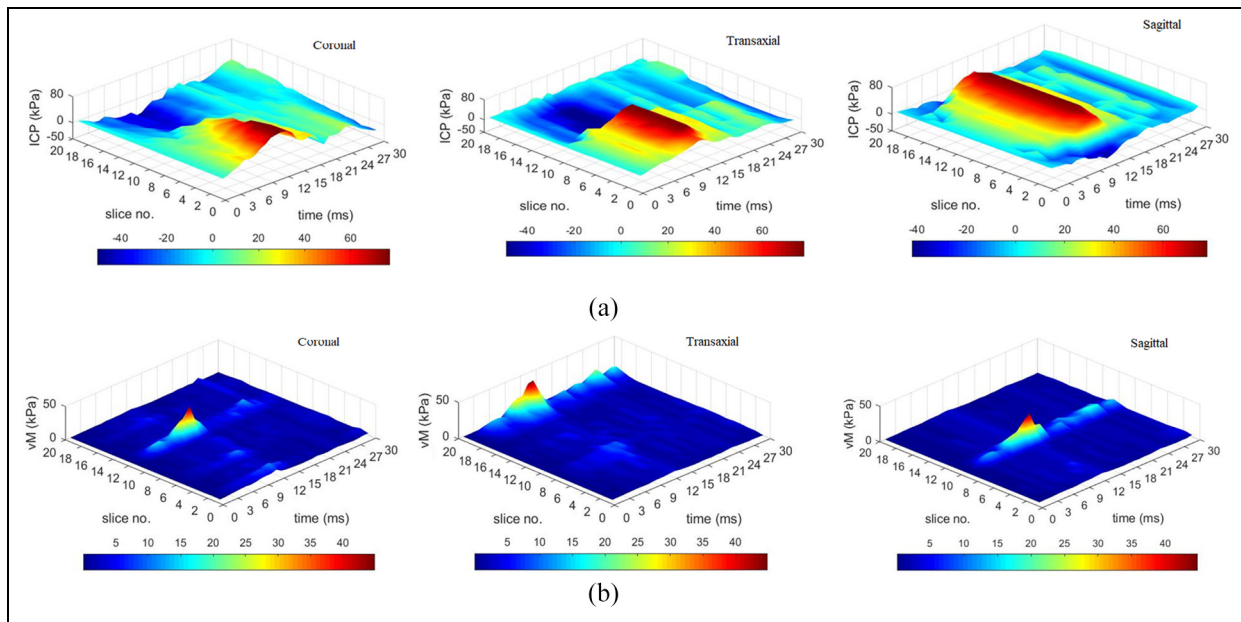
Figure 13. Illustration of the time evolution of (a) maximum ICP and (b) vM distribution with the position of brain cross-sectional slices for Case 2.

reported literature.[52] According to Jefferson[56] and Pearce,[57] the regular cellular action disruption in the reticular activating system (RAS) in the brain stem is the furthermost responsible reason for concussion of critical severity. Unlike cerebral contusions, brainstem contusions have critical and high clinical relevance and these cannot be healed without medical interventions.[58] This von Mises stress distribution across the brain (where the maximum value of stress in the brainstem is observed near foramen magnum) coincides qualitatively with the results of experiments performed on monkey.[59] The threshold values for coup ICP, contrecoup ICP, and von Mises stress are presented in correlation with Abbreviated Injury Scale (AIS) score by Yao et al.[60] According to this, the mild concussion–type brain injury (with AIS score 2) occurs beyond 180 kPa mean coup pressure, -122 kPa mean contrecoup pressure, and 11.7 kPa mean von Mises stress. In both the cases presented in the article, the coup pressure lies under the threshold value, whereas the von Mises stress exceeds well beyond the threshold of 11.7 kPa.

In Case 1, the contre-coup pressure is obtained near the threshold of -122 kPa which indicates the chances of mild concussion and contusion in the cerebrum in Case 1 (with AIS 2 score). This results in biological symptoms of confusion, memory loss, and disorientation.[60,61] The literature also reports the dramatic increase in brain injury risk ($>60\%$, AIS $3+$ score) when von Mises stress exceeds beyond 15 kPa.[60] In both the cases presented in the article, von Mises exceeds 15 kPa with a minimum margin of 30 kPa. Hence, the occurrence of severe TBI with AIS score of $3+$ is possible, which can lead to hematoma (hemorrhage) and diffuse axonal injury in cerebrum.[61]

Conclusion

A new FE human head model with an accurate representation of gyri and sulci structures in the brain is developed and validated against the two human cadaver impact experiments. The ICP values are used to validate the model in both the cases. A good correlation between simulation and experimental ICP is observed in Nahum's validation study. The results presented in the article are more realistic compared to the validation results presented by some recent advanced FE head model,[27] for the majority of the loading cases. The results for model validation against Trosseille's experiment agreeably coincide with the experimental results in frontal and lateral ventricle region. Time variation of ICP and von Mises stress across brain cross-sectional planes is utilized to study brain injury probability in detail. The ICP surface plots are utilized to analyze the probability of mild TBI, while the von Mises stress plots represented the highly damaged sections of the brain in both the cases studied. The analysis concluded that the frontal region of the brain experienced the highest probability of contusion and concussion, while the brain stem was the most vulnerable section to suffer lacerations. This newly developed, agreeably validated FE human head model can be used to understand the injury mechanisms more evidently and can be used to develop suitable head injury criteria. As the brain surface is modeled accurately in this work, this model can be used for the precise and effective study of contusion and concussions. The present model mainly focuses on the soft tissue surface structure which can be improved with the inclusion of meningeal layers, especially, the thicker dura mater. In addition, this work can be extended to consider the anisotropy of

the brain by segmenting the white and gray matter in cerebrum, cerebellum, and brain stem. The contacts between the segments can be improved to allow the free brain motion inside the skull. The developed model can further be validated against other experimental data presented in previous works[4,35,36] to increase the robustness of the model for precise prediction of the TBI criteria and injury mechanism.

Declaration of conflicting interests

Funding

ORCID iD

Harikrishnan Narayanan Unni   https://orcid.org/0000-0001-8678-7665

References

1. Zhao W, Ruan S and Ji S. Brain pressure responses in translational head impact: a dimensional analysis and a further computational study. *Biomech Model Mechanobiol* 2015; 14: 753–766.
2. Siswanto WA and Hua CS. Strength analysis of human skull on high speed impact. *Int Rev Mech Eng* 2012; 6(7): 1508–1514.
3. Yan W and Pangestu OD. A modified human head model for the study of impact head injury. *Comput Methods Biomech Biomed Eng* 2011; 14: 1049–1057.
4. Yoganandan N and Pintar FA. Biomechanics of temporo-parietal skull fracture. *Clin Biomech* 2004; 19: 225–239.
5. Kleiven S. Influence of impact direction on the human head in prediction of subdural hematoma. *J Neurotrauma* 2003; 20: 365–379.
6. Tabish SA and Syed N. Recent advances and future trends in traumatic brain injury. *Emerg Med Open Access* 2015; 5: 1.
7. Lopez AD, Mathers CD, Ezzati M, et al. Global and regional burden of disease and risk factors, 2001: systematic analysis of population health data. *Lancet* 2006; 367: 1747–1757.
8. King AI, Ruan JS, Zhou C, et al. Recent advances in biomechanics of brain injury research: a review. *J Neurotrauma* 1995; 12: 651–658.
9. Tse KM, Lim SP, Beng V, et al. A review of head injury and finite element head models. *Am J Eng Technol Soc* 2014; 1: 28–52.
10. Afshari J, Haghpanahi M and Kalantarinejad R. Developing new brain injury criteria for predicting the intracranial response by calculating von Mises stress, coup pressure and contrecoup pressure. *J Brazilian Soc Mech Sci Eng* 2017; 39: 3729–3741.
11. El Sayed T, Mota A, Fraternali F, et al. Biomechanics of traumatic brain injury. *Comput Methods Appl Mech Eng* 2008; 197: 4692–4701.
12. Pearce CW and Young PG. On the pressure response in the brain due to short duration blunt impacts. *PLoS ONE* 2014; 9: e0114292.
13. Laksari K, Kurt M, Babaee H, et al. Mechanistic insights into human brain impact dynamics through modal analysis. *Phys Rev Lett* 2018; 120: 138101.
14. Levadnyi I, Awrejcewicz J, Zhang Y, et al. Finite element analysis of impact for helmeted and non-helmeted head. *J Med Biol Eng* 2017; 38: 587–595.
15. Anzelius A. The effect of an impact on a spherical liquid mass. *Acta Pathol Microbiol Scand* 1943; 48: 153–159.
16. Ward CC, Chan M and Nahum AM. Intracranial pressure—a brain injury criterion. In: *Proceedings of the 24th Stapp Car Crash Conference*, Troy, MI, 15–17 October 1980. USA: SAE International.
17. Kabo JM and Goldsmith W. Response of a human head-neck model to transient saggital plane loading. *J Biomech* 1983; 16: 313–321.
18. Khalil TB and Hubbard RP. Parametric study of head response by finite element modeling. *J Biomech* 1977; 10: 119–132.
19. Wahi KK and Merchant HC. Mechanical response of a head injury model with viscoelastic brain tissue. *Ann Biomed Eng* 1977; 5: 303–321.
20. Horgan TJ and Gilchrist MD. The creation of three-dimensional finite element models for simulating head impact biomechanics. *Int J Crashworthiness* 2003; 8: 353–366.
21. Kleiven S. Predictors for traumatic brain injuries evaluated through accident reconstructions. *Stapp Car Crash J* 2007; 51: 81–114.
22. Mao H, Zhang L, Jiang B, et al. Development of a finite element human head model partially validated with thirty five experimental cases. *J Biomech Eng* 2013; 135: 111002.
23. Ruan JS, Khalil T and King AI. Dynamic response of the human head to impact by three-dimensional finite element analysis. *J Biomech Eng* 2008; 116: 44–50.
24. Takhounts EG, Ridella SA, Hasija V, et al. Investigation of traumatic brain injuries using the next generation of simulated injury monitor (SIMon) finite element head model. *Stapp Car Crash J* 2008; 52: 1–31.
25. Zhang L, Yang K, Dwarampudi R, et al. Recent advances in brain injury research: a new human head model development and validation. *Stapp Car Crash* 2001; 45: 369–394.
26. Yang B, Tse KM, Chen N, et al. Development of a finite element head model for the study of impact head injury. *Biomed Res Int* 2014; 2014: 408278.
27. Fernandes FAO, Tchepel D, Alves de Sousa RJ, et al. Development and validation of a new finite element human head model: yet another head model (YEAHM). *Eng Comput (Swansea, Wales)*. Epub ahead of print 2018. DOI: 10.1108/EC-09-2016-0321.
28. Nahum AM, Smith RW and Ward CC. Intracranial pressure dynamics during head impact. In: *Proceedings of the 21st Stapp Car Crash Conference*, New Orleans, LA, 19–21 October 1977, pp. 339–366. USA: SAE International.
29. Ruan J and Prasad P. The effects of skull thickness variations on human head dynamic impact responses. *Stapp Car Crash J* 2001; 45: 395–414.

30. Rashid B, Destrade M and Gilchrist M. Mechanical characterization of brain tissue in compression at dynamic strain rates. *J Mech Behav Biomed Mater* 2012; 10: 23–38.

31. Prosser JD, Vender JR and Solares CA. Traumatic cerebrospinal fluid leaks. *Otolaryngol Clin North Am* 2011; 44: 857–873.

32. Gennarelli TA. Mechanisms of brain injury. *J Emerg Med* 1993; 11: 5–11.

33. Trosseille X, Tarriere C, Lavaste F, et al. Development of a FEM of the human head according to a specific test protocol. In: *Proceedings of the 36th Stapp Car Crash Conference*, Ponte Verdra Beach, FL, 2–4 November 1992. USA: SAE International.

34. Hardy WN, Foster CD, Mason MJ, et al. Investigation of head injury mechanisms using neutral density technology and high-speed biplanar X-ray. *Stapp Car Crash J* 2001; 45: 337–368.

35. Marjoux D, Baumgartner D, Deck C, et al. Head injury prediction capability of the HIC, HIP, SIMon and ULP criteria. *Accid Anal Prev* 2008; 40: 1135–1148.

36. Hardy WN, Mason MJ, Foster CD, et al. A study of the response of the human cadaver head to impact. *Stapp Car Crash J* 2007; 51: 17–80.

37. Horgan TJ and Gilchrist MD. Influence of FE model variability in predicting brain motion and intracranial pressure changes in head impact simulations. *Int J Crashworthiness* 2004; 9: 401–418.

38. Willinger R, Kang HS and Diaw B. Three-dimensional human head finite-element model validation against two experimental impacts. *Ann Biomed Eng* 1999; 27: 403–410.

39. Shuck LZ and Advani SH. Rheological response of human brain tissue in shear. *J Basic Eng* 1972; 94: 905–911.

40. Yoganandan N, Pintar FA, Zhang J, et al. Physical properties of the human head: mass, center of gravity and moment of inertia. *J Biomech* 2009; 42: 1177–1192.

41. Suwatcharangkoon S, Meyers E, Falo C, et al. Loss of consciousness at onset of subarachnoid hemorrhage as an important marker of early brain injury. *JAMA Neurol* 2016; 73: 28–35.

42. Baumgartner D and Willinger R. Human head tolerance limits to specific injury mechanisms inferred from real world accident numerical reconstruction. *Rev Eur Des Éléments Finis* 2005; 14: 421–443.

43. Lee B and Newberg A. Neuroimaging in traumatic brain imaging. *NeuroRx* 2005; 2: 372–383.

44. Micheau ADH. *Anatomy of the brain (MRI)—cross-sectional atlas of human anatomy*. Montpellier: IMAIOS.

45. Allen JS, Damasio H and Grabowski TJ. Normal neuroanatomical variation in the human brain: an MRI-volumetric study. *Am J Phys Anthropol* 2002; 118: 341–358.

46. Gilchrist MD. Modelling and accident reconstruction of head impact injuries. *Key Eng Mater* 2003; 245–246: 417–432.

47. Boulanger P and Hayes MA. Finite amplitude waves in Mooney–Rivlin and Hadamard materials. In: Hayes MA and Soccomandi G (eds) *Topics in finite elasticity*, Vol. 424. Vienna: Springer, 2001, pp. 131–167.

48. Deck C and Willinger R. Head injury predictive tools for protective systems optimisation. In: *7th European LS-DYNA conference*, Salzburg, 14–15 May 2009. DYNAmore GmbH.

49. Ogden RW. Large deformation isotropic elasticity: on the correlation of theory and experiment for compressible rubberlike solids. *Proc R Soc A Math Phys Eng Sci* 1972; 328: 567–583.

50. Kleiven S. Why most traumatic brain injuries are not caused by linear acceleration but skull fractures are. *Front Bioeng Biotechnol* 2013; 1: 15.

51. Zhang L, Yang KH and King AI. A proposed injury threshold for mild traumatic brain injury. *J Biomech Eng* 2004; 126: 226–236.

52. Willinger R and Baumgartner D. Numerical and physical modelling of the human head under impact—towards new injury criteria. *Int J Vehicle Design* 2003; 32: 1–2.

53. Arbogast KB and Margulies SS. Material characterization of the brainstem from oscillatory shear tests. *J Biomech* 1998; 31(9): 801–807.

54. Prange MT and Margulies SS. Regional, directional, and age-dependent properties of the brain undergoing large deformation. *J Biomech Eng* 2002; 124(2): 244–252.

55. Hrapko M. The influence of test conditions on characterization of the mechanical properties of brain tissue. *J Biomech Eng* 2008; 130(3): 031003.

56. Jefferson G. The nature of concussion. *BMJ* 1944; 1(4330): 1–5.

57. Pearce JM. Observations on concussion: a review. *Eur Neurol* 2008; 59(3–4): 113–119.

58. Khoshyomn S and Tranmer BI. Diagnosis and management of pediatric closed head injury. *Semin Pediatr Surg* 2004; 13(2): 80–86.

59. Antona MJ. *Traumatic brain injuries: animal experiments and numerical simulations to support the development of a brain injury criterion*. PhD Thesis, Chalmers University of Technology, Gothenburg, 2016.

60. Yao J, Yang J and Otte D. Investigation of head injuries by reconstructions of real-world vehicle-versus-adult-pedestrian accidents. *Safety Sci* 2008; 46(7): 1103–1114.

61. Carroll CP, Cochran JA, Price JP, et al. The AIS-2005 revision in severe traumatic brain injury: mission accomplished or problems for future research? *Ann Adv Automot Med* 2010; 54: 233–238.